

# Open Research Online

---

The Open University's repository of research publications and other research outputs

## High-cadence spectroscopy of M dwarfs – I. Analysis of systematic effects in HARPS-N line profile measurements on the bright binary GJ 725A+B

### Journal Item

#### How to cite:

Berdiñas, Z. M.; Amado, P. J.; Anglada-Escudé, G.; Rodríguez-López, C. and Barnes, J. (2016). High-cadence spectroscopy of M dwarfs – I. Analysis of systematic effects in HARPS-N line profile measurements on the bright binary GJ 725A+B. *Monthly Notices of the Royal Astronomical Society*, 459(4) pp. 3551–3564.

For guidance on citations see [FAQs](#).

© 2016 The Authors

Version: Version of Record

Link(s) to article on publisher's website:  
<http://dx.doi.org/doi:10.1093/mnras/stw906>

---

Copyright and Moral Rights for the articles on this site are retained by the individual authors and/or other copyright owners. For more information on Open Research Online's data [policy](#) on reuse of materials please consult the policies page.

---

[oro.open.ac.uk](http://oro.open.ac.uk)

# High-cadence spectroscopy of M dwarfs – I. Analysis of systematic effects in HARPS-N line profile measurements on the bright binary GJ 725A+B

Z. M. Berdiñas,<sup>1,2\*</sup> P. J. Amado,<sup>1</sup> G. Anglada-Escudé,<sup>3,4</sup> C. Rodríguez-López<sup>1</sup> and J. Barnes<sup>5</sup>

<sup>1</sup>*Instituto de Astrofísica de Andalucía – CSIC, Glorieta de la Astronomía S/N, E-18008 Granada, Spain*

<sup>2</sup>*Universidad de Granada – PhD Program in Physics and Mathematics (FisyMat), E-18071 Granada, Spain*

<sup>3</sup>*School of Physics and Astronomy, Queen Mary University of London, 327 Mile End Rd, London E1 4NS, UK*

<sup>4</sup>*Centre for Astrophysics Research, University of Hertfordshire, College Lane, Hatfield, Herts AL10 9AB, UK*

<sup>5</sup>*Department of Physical Sciences, The Open University, Walton Hall, Milton Keynes MK7 6AA, UK*

Accepted 2016 April 14. Received 2016 April 5; in original form 2016 February 26

## ABSTRACT

Understanding the sources of instrumental systematic noise is a must to improve the design of future spectrographs. In this study, we alternated observations of the well-suited pair of M-stars GJ 725A+B to delve into the sub-night High Accuracy Radial Velocity Planet Searcher for the Northern hemisphere (HARPS-N) response. Besides the possible presence of a low-mass planet orbiting GJ 725B, our observations reveal changes in the spectral energy distribution (SED) correlated with measurements of the width of the instrumental line profile and, to a lower degree, with the Doppler measurements. To study the origin of these effects, we searched for correlations among several quantities defined and measured on the spectra and on the acquisition images. We find that the changes in apparent SED are very likely related to flux losses at the fibre input. Further tests indicate that such flux losses do not seriously affect the shape of the instrumental point spread function of HARPS-N, but identify an inefficient fitting of the continuum as the most likely source of the systematic variability observed in the full width at half-maximum. This index, accounting for the HARPS-N cross-correlation profiles width, is often used to decorrelate Doppler time series. We show that the Doppler measurement obtained by a parametric least-squares fitting of the spectrum accounting for continuum variability is insensitive to changes in the slope of the SED, suggesting that forward modelling techniques to measure moments of the line profile are the optimal way to achieve higher accuracy. Remaining residual variability at  $\sim 1 \text{ m s}^{-1}$  suggests that for M-stars Doppler surveys the current noise floor still has an instrumental origin.

**Key words:** instrumentation: spectrographs – techniques: radial velocities – stars: individual: GJ 725A – stars: individual: GJ 725B – stars: low-mass.

## 1 INTRODUCTION

The radial velocity (RV) method to detect extrasolar planets has now reached long-term precisions of  $\sim 1 \text{ m s}^{-1}$ , and new instruments are being built to achieve accuracies in the few tens of  $\text{cm s}^{-1}$  regime (e.g. ESPRESSO; Pepe et al. 2010). A thorough understanding of the current instruments and their standard extraction, reduction and RV determination pipelines is essential in achieving their ultimate capabilities, and identifying the key technical aspects that need refinement in the next generation of instruments. While  $1 \text{ m s}^{-1}$  precision has been enough to identify the emerging popu-

lation of super-Earths in compact planetary systems, and to detect potentially habitable planets around M dwarfs, achieving sub- $\text{m s}^{-1}$  precision at all time-scales is needed to efficiently characterize Earth and sub-Earth mass objects in hot-to-warm orbits around G and K dwarfs. There is active discussion on whether the reported  $\sim 1 \text{ m s}^{-1}$  long-term precision limit, measured on stabilized spectrographs, is caused by stellar processes, instrumental effects or both. While certain stars are, intrinsically, more Doppler variable than this limit, it is unlikely that the  $0.8\text{--}0.9 \text{ m s}^{-1}$  (reported lower noise limit in HARPS-ESO observations by Pepe et al. 2011, and of a handful of very quiet M dwarfs, e.g. GJ 699 and GJ 588, by Anglada-Escudé & Butler 2012) is a universal limit for Doppler measurements.

Studying the limits of precision of Doppler spectroscopy in the short period domain of M-type dwarfs is one of the primary goals

\*E-mail: [zaira@iaa.es](mailto:zaira@iaa.es)

of the ‘Cool Tiny Beats survey’ (CTB; Anglada-Escudé et al. 2014; Berdiñas, Amado & Anglada-Escudé 2015). The survey, started in 2013, was designed to obtain high-cadence observations (continuous observing of a single target during several consecutive nights) of a small sample of M dwarfs with HARPS-ESO (High Accuracy Radial Velocity Planet Searcher, installed on ESO’s 3.6 m telescope at La Silla Observatory in Chile) and HARPS-N (High Accuracy Radial Velocity Planet Searcher for the Northern hemisphere; Mayor et al. 2003; Pepe et al. 2004; Cosentino et al. 2012). Our objective was threefold: (1) the detection of small planets in sub-day period orbits, (2) the search for pulsations, and (3) the study of the time-scales of stellar activity.

From the analysis of those data, it was obvious that some kind of instrumental or reduction-process effect was producing intranight and night-to-night variability common to several targets. After the first runs in each instrument, two of such effects were quickly identified: (1) Doppler shift correlations with the signal-to-noise ratio (SNR; Bouchy et al. 2009), and (2)  $\sim 0.5$ – $1.5$  m s $^{-1}$  night-to-night jumps in the RV series. Berdiñas et al. (in preparation; hereafter, CTB 2016) find that the first one was partly due to the charge-transfer-efficiency effect, and provide an empirical correction that should at least be valid for M dwarfs observed from HARPS-ESO. The effect was corrected in HARPS-N (but not in HARPS-ESO) by introducing, in 2013, modifications to the standard Data Reduction Software (DRS) pipeline (Lovis & Pepe, private communication). The second effect was found to be caused by random and systematic errors in the wavelength solution of unknown origin (Lo Curto, private communication). CTB 2016 also provide a solution for this effect that consists in using a mean wavelength solution for each observing run instead of the one derived from individual night calibrations, for both HARPS-ESO and HARPS-N.

While these corrections substantially reduced the common systematic variability of several observed stars, yet another source of systematic noise was strongly affecting HARPS-N data of M-dwarf stars. This variability correlates with the airmass, and was found to produce structured Doppler noise at the level of  $\sim 2$  m s $^{-1}$ , with even larger amplitude in the full width at half-maximum (FWHM) of the cross-correlation function (CCF). Similar trends have been recently reported for circular fibre-fed spectrographs like SOPHIE for other spectral types (Böhm et al. 2015).

There are many environmental effects which worsen the higher the airmass is, such as the atmospheric refraction, which increases with the air density at low altitudes splitting the star image in its blue–red components in the zenithal direction; the seeing, which also increases at low altitudes, being the blurring more severe for shorter wavelengths; or the atmospheric extinction, caused by the Rayleigh scattering and by the molecules and dust absorption. In terms of airmasses, the atmospheric dispersion dominates below  $\sim 50$  deg on nights with good seeing ( $\sim 1$  arcsec in the zenith). To correct for this, HARPS-N includes an atmospheric dispersion corrector (ADC).

The aim of this work is to study the response of the instrument to any of these sources in the intranight regime, check if these effects lead to variability of the spectra and provide means for correcting them. The paper is organized as follows. We describe the observations and the properties of the targets used for this study (GJ 725A and B) in Section 2. The data reduction and the spectroscopic and image indices to be used in this study are presented in Section 3. Section 4 comprises the analysis, where, in Section 4.1 we show the common variability detected in the alternating observations between GJ 725A and B, and also we intend to assess statistical correlations between spectroscopic observables and var-

ious instrument related quantities. In Section 4.2 we introduce the least-squares deconvolution (LSD) profiles and perform two experiments to test the algorithms used in this paper (HARPS-TERRA and DRS data reduction softwares). We propose tentative functions to detrend the line width and the RV measurements in Section 4.3. In Section 4.4 we present the analysis of the mean line profiles calculated in the cross-dispersed direction. We discuss a promising  $\sim 2.7$ -d Doppler signal in GJ 725B in Section 4.5. Finally, Section 5 presents the discussion and conclusions of this work.

## 2 OBSERVATIONS

We used the HARPS-N spectrograph at the 3.6 m Telescope Nazionale Galileo (TNG), settled at the Roque de los Muchachos Observatory (ORM) in La Palma. HARPS-N is nearly a twin of HARPS-ESO. To guarantee that the optics keep their alignment, both are vacuum-sealed thermally stabilized fibre-fed échelle spectrographs. HARPS-N input fibre samples 1-arcsec circular apertures on the sky, producing high-resolution optical spectra from 383 up to 693 nm. The high resolution  $R \sim 120\,000$  (at the central wavelength, see table 6 in Cosentino et al. 2012), makes the RVs measured from the spectra the most long-term accurate currently available.

Our targets were the bright nearby stars: GJ 725A and GJ 725B.<sup>1</sup> We selected this binary system for being a bright ( $V = 8.91$  and  $9.69$ , for A and B, respectively; Jenkins et al. 2009), nearby ( $d = 3.57$  and  $3.45$  pc; Anderson & Francis 2012) and common proper motion pair of almost identical spectral type (M3V and M3.5V; Reid, Hawley & Gizis 1995) with no previous reports of intense magnetic activity or planets. At epoch 2000, their projected separation was  $13.3$  arcsec, implying a minimum separation of  $47.5$  au (Hipparcos; van Leeuwen 2007).

We observed the stars in two high-cadence different runs, one in 2013 and another one in 2014. GJ 725A was the primary target of our five-day long, 2013 August run, whereas, in 2014, GJ 725A and B were observed every night for four consecutive nights alternating exposures between the two of them. This gave us a total of 314 A data points in 2013 and 101 for A and 116 for B in 2014, after rejecting those with SNR below 45 and airmass above 2.5 (the HARPS-N atmospheric corrector does not work for higher airmasses; Pepe, private communication). In the 2014 run, except for the first night, we halted the alternating sequence between A and B at the meridian passage, observing instead only one of the stars. We did this to improve the cadence of each target at that specific moment of the night. Exposure times were set to be between 240 and 480 s. The main observational parameters of the run are shown in Table 1.

## 3 MEASUREMENTS

For each observation, we obtained a number of measurements (or indices; see in Table 2, a portion of these measurements) to perform this study. These indices are detailed below.

### 3.1 Spectroscopic measurements

Spectra were processed and extracted with the standard HARPS-N/TNG Data Reduction Software (DRS). We obtained the RV

<sup>1</sup> Check <http://www.pas.rochester.edu/~emamajek/spt/M3V.txt> and <http://www.pas.rochester.edu/~emamajek/spt/M3.5V.txt> for a thorough review of both stars properties.

**Table 1.** Observational parameters of the 2014 run.

Nights	Night 1	Night 2	Night 3	Night 4
$N_A$	27	40	16	18
$N_B$	27	21	31	37
$AM_{\max}$	1.55	1.64	1.59	1.65
Seeing	0.86	0.87	0.74	0.78
Seeing <sub>min</sub>	0.58	0.60	0.48	0.59
Seeing <sub>max</sub>	2.83	1.47	3.64	1.20
SNR <sub>A</sub>	78	54	59	71
SNR <sub>B</sub>	63	49	53	59

*Notes.* Main observational parameters of the 2014 run (July 2–5). Sub-indices A and B refer to targets GJ 725A and GJ 725B.  $N$  indicates the number of exposures. The SNR and seeing values are median measurements of the nights. SNR values correspond to the spectral order 60, centred at 631 nm. Since the TNG seeing monitor was out of order, we show the values given by the nearby Isaac Newton Telescope. 1.17 was the minimum airmass (AM) of all nights.

measurements using the maximum likelihood matching technique implemented in the HARPS-TERRA software (Anglada-Escudé & Butler 2012).

The DRS cross-correlates the observed spectra with a weighted binary mask formed by ones in the theoretical stellar lines positions and widths and by zeros elsewhere (Pepe et al. 2002). The resulting CCF acts as a proxy for the mean line profile for each spectral order. In our study, we will use the so-called FWHM index (FWHM of the Gaussian fitted to the cross-correlation profile). Since the line width might be sensitive to the presence of spots or magnetic activity (e.g. Reiners et al. 2013), this FWHM is often used as an activity index to decorrelate Doppler variability.

### 3.2 Spectral energy distribution measurements (pSEDs and $K$ -index)

We also studied the distribution of the flux across the spectra. With this aim, we used the spectra as given by the DRS reduction pipeline for each spectral order (the so-called e2ds data-products), and we calculated how the total flux on each spectral order varied relative to a reference order. To do this, we first added the flux of all pixels in each spectral order, and secondly, we normalized these measure-

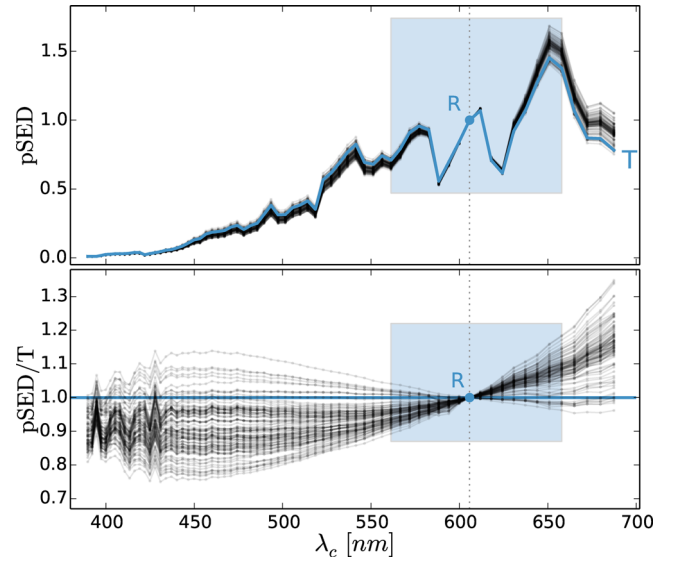


**Figure 1.** (Upper panel) Sum of the flux of the 69 spectral orders of GJ 725A (the so-called pseudo spectral energy distribution, pSED) plotted versus wavelength ( $\lambda_c$  refers to the central wavelength of each spectral order). The pSEDs cross the normalization point (R). The blue line T indicates the initial pSED of the run. (Lower panel) Relative flux compared to T. We limited the study to a linear pSED/T region of  $\pm 8$  spectral orders from R (blue area). Fluxes were corrected from atmospheric extinction.

ments to the total flux at the spectral order 56, which was selected for having low telluric contamination. We named this ‘normalized pseudo spectral energy distribution’ (pSED). As we see for the 2014 data of GJ 725A in the upper panel of Fig. 1, the pSED pivots around the normalization order (R). Changes relative to the first co-added spectrum (T) are shown in the lower panel of Fig. 1.

The pSED is expected to vary for a number of environmental effects coupled with the instrument, as for example the atmospheric dispersion or the chromatic seeing. Account for the atmospheric dispersion is the ADC role; however, the flux reaching the telescope will also change as a function of airmass due to the atmospheric extinction (i.e. due to the Rayleigh scattering and to the absorption from molecules and dust in the Earth atmosphere). We corrected

**Table 2.** Radial velocities observed for GJ 725A and GJ 725B with HARPS-N. The columns are as follows: barycentric Julian date, RVs calculated with HARPS-TERRA and their error bars, FWHM of the cross-correlation function, signal-to-noise at the spectral order centred at 631 nm, airmass, the  $\Phi$  and  $\Theta$  indices obtained from the autoguide camera images, the  $K$ -index measured over the spectra, the FWHM and the RV corrected from intranight systematics.

Object	BJD	RV (m s <sup>-1</sup> )	FWHM (m s <sup>-1</sup> )	SNR (at 631 nm)	AM (arcsec)	$\Phi$ (pxl)	$\Theta$ (arcsec)	$K$ ( $\mu\text{m}^{-1}$ )	FWHM <sub>real</sub> <sup>2</sup> (m s <sup>-1</sup> ) <sup>2</sup>	RV <sub>C</sub> (m s <sup>-1</sup> )
GJ 725A	2456518.36	0.88	3024.13	66.48	1.22	–	–	0.00	3024.13	0.88
	2456518.37	1.42	3030.39	72.79	1.22	–	–	–0.34	3026.87	1.18
	2456518.37	1.98	3030.63	63.74	1.21	–	–	–0.50	3025.55	1.63
	...	...	...	...	...	...	...	...	...	...
	2456841.39	–0.71	3002.59	67.28	1.55	6.85	–0.04	0.68	3009.60	–
	2456841.40	–0.86	2996.76	65.87	1.48	6.93	0.00	1.26	3009.73	–
GJ 725B	2456841.41	–0.36	2991.07	53.23	1.42	7.85	0.00	1.76	3009.26	–
	...	...	...	...	...	...	...	...	...	...
	2456841.39	–0.46	2984.25	52.24	1.51	7.24	0.01	0.66	2991.11	–
	2456841.40	–0.24	2985.22	59.62	1.45	6.70	–0.05	0.75	2993.00	–
	2456841.42	–0.63	2978.01	58.27	1.39	6.58	0.09	1.50	2993.54	–
	...	...	...	...	...	...	...	...	...	...

*Notes.* This table is available in its entirety in a machine-readable form as online Supporting Information. A portion is shown here for guidance regarding its form and content.

the pSED due to atmospheric extinction using the method outlined by Hayes & Latham (1975).<sup>2</sup> Although the atmospheric extinction is wavelength and airmass dependent, the pSED varied less than a 4.5 per cent and the wavelength dependence in the pSED remained equally strong after the correction.

To quantify the impact of changes in the pSED, we defined a spectroscopic chromatic index ( $K$ ).  $K$ -index accounts for changes in the slope of the pSED depending on the wavelength. We calculated  $K$  by fitting a linear trend in wavelength range which surround  $R$  (orders inside the blue box of Fig. 1). Then,  $K$  was obtained from:

$$\text{pSED}_t(\lambda) = [1 + K_t(\lambda_c - \lambda_{cR})] T(\lambda), \quad (1)$$

where  $t$  indicates the observations,  $\lambda_{cR}$  is the central wavelength of the reference order 56,  $\lambda_c$  refers to the central wavelength of any other order,  $T(\lambda)$  corresponds to the initial  $\text{pSED}_{i0}(\lambda)$  for each star and, finally,  $K_t$  is a coefficient with units of  $1/\lambda$ , that we call chromatic index.

### 3.3 Measurements on the autoguide camera images (semimajor axis module, $\Phi$ , and circularity index, $\Theta$ )

The images obtained by the autoguide camera were additional products that were used for trying to find an explanation for the systematics. In HARPS-N, the star light that is not injected into the fibre is reflected towards the autoguide camera. To do this, the fibre head is fitted in the central hole of a slightly tilted flat mirror. Therefore, the images recorded by this camera show the shape of the star at the fibre entrance. Two kind of images are stored, the acquisition images, taken with the star off-fibre before the science exposure, and the autoguide images, which are the average of the short images ( $\sim 100$  ms) taken during the science exposure to guide the telescope.

It must be realized that, in an equatorial telescope (or in a derotated field of view in an altazimuthal telescope), the direction of the dispersion of the atmosphere changes during the night (following the zenithal direction), whereas in a non-derotated field of view (the case of HARPS-N@TNG) the zenithal direction remains constant while the field rotates (see Fig. 2).

It is important to note that, as a result of the flat mirror tilt, a stable distortion of the images was expected; i.e. we expected the images to be elongated in the same proportion and direction as we measured for the circular hole of the mirror (see the shape of the central hole in Fig. 3). However, the autoguide images presented a variable elliptical elongated shape of the star that did not fit the distortion of the mirror hole and did not rotate with the field (within a maximum error of  $4^\circ$ ), keeping always aligned with the zenithal direction. This result, together with the correlation of the elongation with the airmass (see three autoguide images taken at the beginning, middle and end of one night, with airmasses 1.30, 1.17 and 1.33, respectively, in Fig. 3), led us to hypothesize that the elongated shape was produced due to an insufficient correction of the atmospheric chromatic dispersion by the ADC. To validate our hypothesis, we fitted an ellipse to the autoguide images (only the outermost pixels with fluxes within  $\pm 1$  per cent of the half value between the maximum and the background were considered), and we checked that the elongation was compatible with the zenithal axis. In particular,

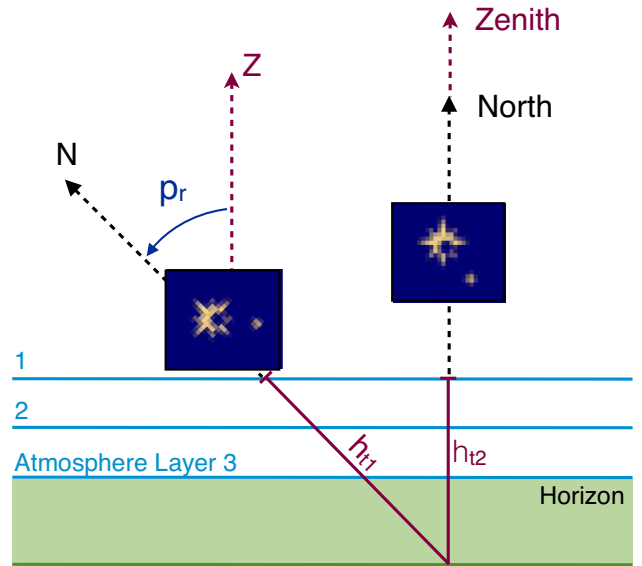


**Figure 2.** Schematic view of the sky orientation of a non-derotated field of view in an altazimuthal telescope like HARPS-N. During the night, the field rotates following the celestial north axis direction (N), while the zenithal axis (Z) remains perpendicular to the atmosphere and does not rotate with the field. The atmosphere chromatically disperses the light more efficiently when the atmospheric layers are thicker (e.g. for  $h_{t1}$  compared with  $h_{t2}$ ).  $p_r$  refers to the parallactic angle, the angle subtended by Z and N.

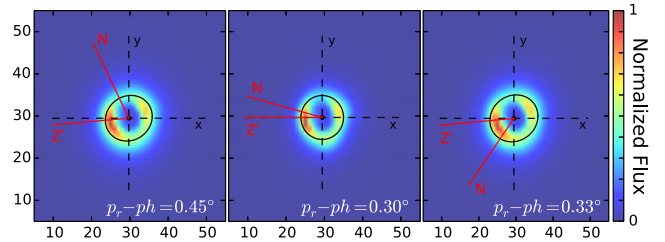


**Figure 3.** GJ 725A autoguide camera images taken at the beginning (left), close to the meridian crossing (middle), and at the end (right) of the 2014 July 2 night. The central hole, which corresponds to the fibre position, seems to be elliptical due the slight tilt of the flat mirror which diverts the light towards the autoguide camera. The solid black lines refers to the elliptical fits performed to account for the elongation of the images. After accounting for the field rotation and the fix angle of the derotator, we measured a good agreement of  $p_h$  – the angle subtended by the north axis N, and the ellipse semimajor axis  $Z'$  – with  $p_r$ , the real parallactic angle (or angle subtended by the north–zenith axis). The distortion of the images is aligned with the atmospheric dispersion axis (Z), and, thus, with the airmass.

we measured maximum differences of only  $7.8 \pm 6.2$  between  $p_r$ , the real parallactic angle, and  $p_h$ , its analogous in case the semimajor axis of the ellipse fitted to the image and the zenithal direction were coincident. Furthermore, if this is so, the resulting image is consistent with a superposition of wavelength-dispersed images of the star caused by the atmosphere.

### 3.4 Summary of used measurements

For the sake of clarity, we summarize here the measurements that will be used in this study.

(i) Spectra:

RV – extracted with HARPS-TERRA.

FWHM – given by the DRS pipeline.

<sup>2</sup> See ORM atmospheric extinction values for a dust-free atmosphere at [http://www.ing.iac.es/Astronomy/observing/manuals/ps/tech\\_notes/tn031.pdf](http://www.ing.iac.es/Astronomy/observing/manuals/ps/tech_notes/tn031.pdf). To correct from aerosol scattering we used the V-band extinction measurements for the month of July from table 1 of García-Gil, Muñoz-Tuñón & Varela (2010).



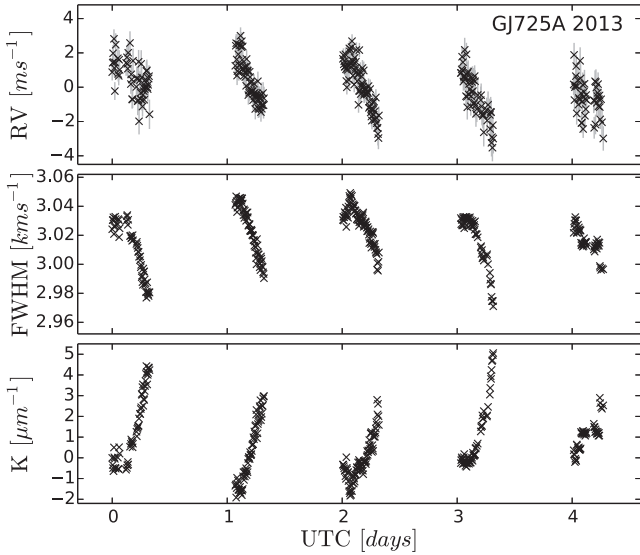


**Figure 4.** RV (top), FWHM (middle) and  $K$  (bottom) time series of GJ 725A observed during five nights run of 2013. The FWHM vary tens of  $\text{m s}^{-1}$  peak-to-peak, while the RV peak-to-peak variability is  $\sim 4.5 \text{ m s}^{-1}$ .

(ii) Spectral energy distribution:

*Spectroscopic chromatic index ( $K$ )* – quantifies the changes in the slope of the SED.

(iii) Autoguide images:

*Semimajor axis module ( $\Phi$ )* – module of the semimajor axis resulting from fitting an ellipse to the autoguide images.

*Circularity index ( $\Theta$ )* – seeing difference, in arcseconds, between the  $x$ - and  $y$ -axis, obtained from the autoguide image headers.

## 4 ANALYSIS

### 4.1 Systematic effects in the time series

GJ 725A was the primary target of the high-cadence 2013 run. These observations showed a clear  $\sim 1$ -d Doppler signal highly correlated with the airmass and common to the RVs and the FWHM time series (see Fig. 4). We suspected an instrumental origin, but with only one observed star, we could not distinguish systematic effects from astrophysical ones.

As a consequence, we designed a second observational run in 2014 to separate astrophysical from instrumental effects: given that GJ 725A+B is a common proper motion pair of almost identical components, obtaining alternating observations of both components is a simple and efficient way to point out common trends. For short periods of time, we also halted the alternation strategy to monitor a single star and increase sensitivity in the high-frequency domain.

Correlated variability, common to both stars, can readily be spotted by direct inspection of the time series (see Fig. 5). For the first observed night, the RV correlation coefficient between GJ 725A and B time series was  $r = 0.30$  and  $0.87$  for the FWHM.

To isolate real signals arising from either star, we computed periodograms of the time series of the individual stars, together with periodograms of their difference (see Fig. 6). Periodograms in Fig. 6 follows the procedures outlined in Zechmeister & Kürster (2009). That is, we used the F-ratio statistic to find what is the period of the sinusoid best-fitting the data (see detailed description in Zechmeister & Kürster 2009). We used these periodograms because, while being formally equivalent to the Lomb–Scargle pe-

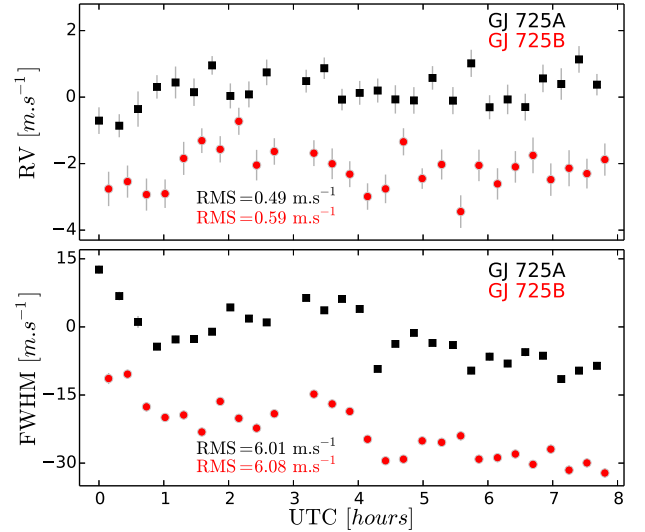


**Figure 5.** GJ 725A (black squares) and GJ 725B (red dots) RVs (upper panel) and FWHM (lower panel) time series for the first HARPS-N run night on 2014 July 2. For the sake of clarity, we subtracted the FWHM mean velocities ( $2989.97$  and  $2975.62 \text{ m s}^{-1}$  for GJ 725A and B, respectively), and we shifted the FWHM ( $-20 \text{ m s}^{-1}$ ) and the RVs ( $-2.3 \text{ m s}^{-1}$ ) of GJ 725B. We referred the time-axis to the beginning of the night at 21 h 11 min 28 s UTC. Both stars show common variability in both quantities confirming an instrumental origin.

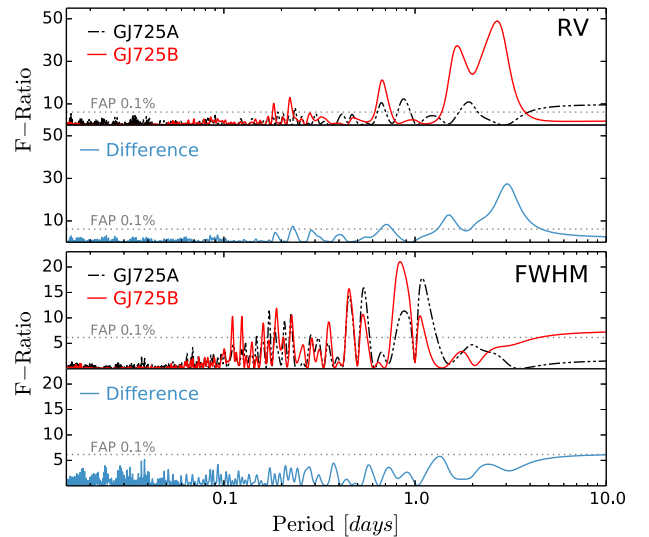


**Figure 6.** Periodograms for the RV (upper panel) and the FWHM (lower panel) for the GJ 725A (black line) and GJ 725B (red line) data of the 2014 run. The blue line corresponds to the periodogram of the two stars differential time series. Note the  $\sim 3$  d peak in the RVs difference over the 0.1 per cent false-alarm-probability threshold. We avoided sampling effects by interpolating the GJ 725B times to the GJ 725A ones. We also excluded high-cadence observations. Common variabilities result in common peaks, which disappear on the differential periodograms. The remaining peaks are real GJ 725A or GJ 725B signals.

riodograms (Scargle 1982), they are less susceptible to aliasing and provide more accurate frequencies. To compute the differential periodograms, we calculated the difference between the GJ 725A and B velocities, evaluating B at the A observing epochs (we linearly interpolate the GJ 725B time series). RV and FWHM periodograms of the individual stars showed common peaks (see black and red

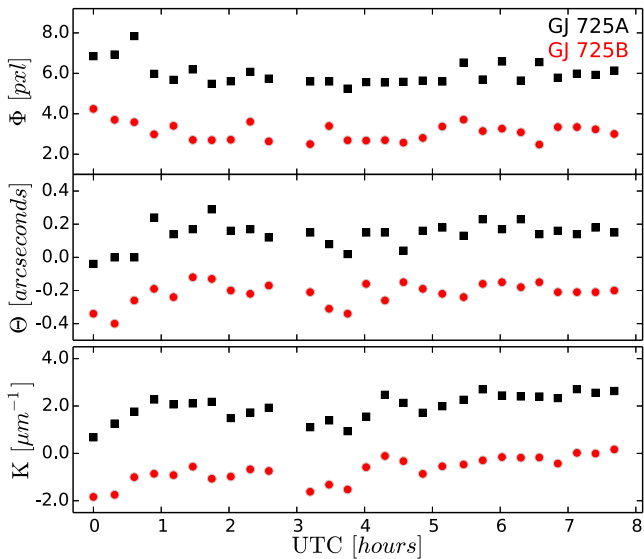


**Figure 7.** Time series of  $\Phi$ ,  $\Theta$  (images indices) and  $K$  (spectroscopic chromatic index) for 2014 July 2. Black squares and red dots correspond to GJ 725A and GJ 725B, respectively. For the sake of clarity, we shifted GJ 725B  $-3$  pxl for  $\Phi$ ,  $-0.35$  arcsec for  $\Theta$  and  $-2.5 \mu\text{m}^{-1}$  for  $K$ . The time axis is referred to the first observation.

lines in Fig. 6), and most of these peaks disappear in the differential periodograms (blue lines). This result suggests common instrumental variability on the data-products of both stars. Note a promising signal arising over the 0.1 per cent of the false-alarm-probability (or FAP; Cumming 2004) threshold at  $\sim 3$  d in the RV differential periodogram. This signal may correspond to some real variability on GJ 725B as we discuss later in Section 4.5. The indices calculated over the autoguide images and the pSED (i.e.  $\Phi$ ,  $\Theta$  and  $K$ ) also show common variability on both stars as we show in Fig. 7.

#### 4.1.1 Analysis of the correlated variability between indices

We analysed all possible correlations between our spectroscopic, autoguide and pSED indices using the following procedure. Given two indices  $x_i$  and  $y_i$ , we modelled the existence of correlations by fitting a linear relation between them:  $y_i = a + bx_i$ , where  $a$  and  $b$  are the free parameters. Assuming that the null model containing no correlation is  $b = 0$  and  $a = \bar{y}$ , our significance assessment consists in obtaining the improvement in the  $\chi^2$  statistic as

$$\Delta\chi^2 = \sum_i \left( \frac{y_i - (a + bx_i)}{\sigma_{y_i}} \right)^2 - \sum_i \left( \frac{y_i - \bar{y}}{\sigma_{y_i}} \right)^2, \quad (2)$$

and then determining whether such an improvement could be caused by a fortunate arrangement in the noise. Instead of using analytic expressions for the expected distribution of  $\Delta\chi^2$  in the presence of noise, we obtained its empirical distribution using a Monte Carlo approach. For each correlation under investigation, we generated a large number of synthetic data sets by randomly swapping the  $y_i$  values while keeping the same  $x_i$ . The FAP is empirically defined here as the number of these random experiments which give a  $\Delta\chi^2$  larger than the one obtained from the real data divided by the total number of experiments. We performed enough experiments (in all cases  $10^3$ – $10^4$  depending on the obtained FAP) to ensure that the FAP estimates were accurate enough.

The correlation analysis for the 2014 measurements (which include both stars) are shown in Figs 8 and 9. The two squares

in the top-right corners of the individual plots indicate the FAP (ticked green squares mean FAP  $< 1$  per cent, dotted orange mean  $1 \text{ per cent} \leq \text{FAP} < 10$  per cent, and crossed red mean FAP  $\geq 10$  per cent) for GJ 725A (black squares data) and GJ 725B (red dots data). We excluded five outliers on  $\Phi$  (three for having a dispersion above 4.5 the measured standard deviation of the sample, and two produced by sudden seeing increases and corresponding SNR in the spectra below 40).

The strongest correlations correspond to the FWHM and the spectroscopic  $K$ -index (Fig. 9, first column). The correlation is so strong that all nights tested resulted in compatible fitted parameters for both stars. This dependence, together with the correlation of  $K$  with the image index  $\Theta$  (Fig. 8, first panel), seems to indicate that the issues at the fibre coupling are propagating all the way down to the science spectrum and affecting its SED and its mean line profile. In other words, the instrumental profile of the spectrograph seems to vary with wavelength and time. It is important to note that variable seeing necessarily increases the autoguide image radius momentarily, but it will increase proportionally in both the  $x$ - and  $y$ -axis. As a result,  $\Theta$  will remain as a good measurement of the asymmetry in the fibre injection.

We also measured a less strong correlation between the RVs and the image index  $\Phi$  (Fig. 8, third panel). We used the GJ 725B RVs after subtracting the Doppler signal discussed in Section 4.5. The correlation is not as strong as that of the FWHM with  $K$ ; however, both stars have the same qualitative behaviour. The FAP of all observed nights remains below the 10 per cent threshold.

#### 4.1.2 Analysis of the 2013 single star run on GJ 725A

Unfortunately, most of the acquisition and some of the guiding images from 2013 were lost due to an error in the acquisition software which was later solved in March 2014.<sup>3</sup> As a result, we could not obtain consistent measurements over the autoguide images.

As for the 2014 alternating run, the analysis shows the  $K$ -index clearly correlated with the FWHM (see Fig. 10). During this run we covered a wider range of airmasses – this study includes data only up to 2.5 in airmass – compared with the 2014 alternating run (which covered up to 1.6 in airmass). This might have been the cause of the larger span of  $K$  values measured in 2013, but a punctual undercorrection of the ADC cannot be ruled out. The slope of the correlation law is equivalent to the value measured on the differential run. The offset could be due to a focus realignment carried out in between the two runs (during the technical run of 2014 March; refer footnote 3).

The wider range of variability in  $K$  seems to better support the existence of a relation between this index and the RVs as well (see Fig. 10, central plot). The variability in both the FWHM and the RV suggested that the mean line profile was changing during the night. However, we could not rule out a problem in the measurements themselves (i.e. in the algorithms) producing spurious variability in the time series. To address this, we performed a number of tests and applied profile measurements independent from the DRS in the next section.

<sup>3</sup> Instrument upgrades can be consulted in <http://www.tng.iac.es/instruments/harpos/>

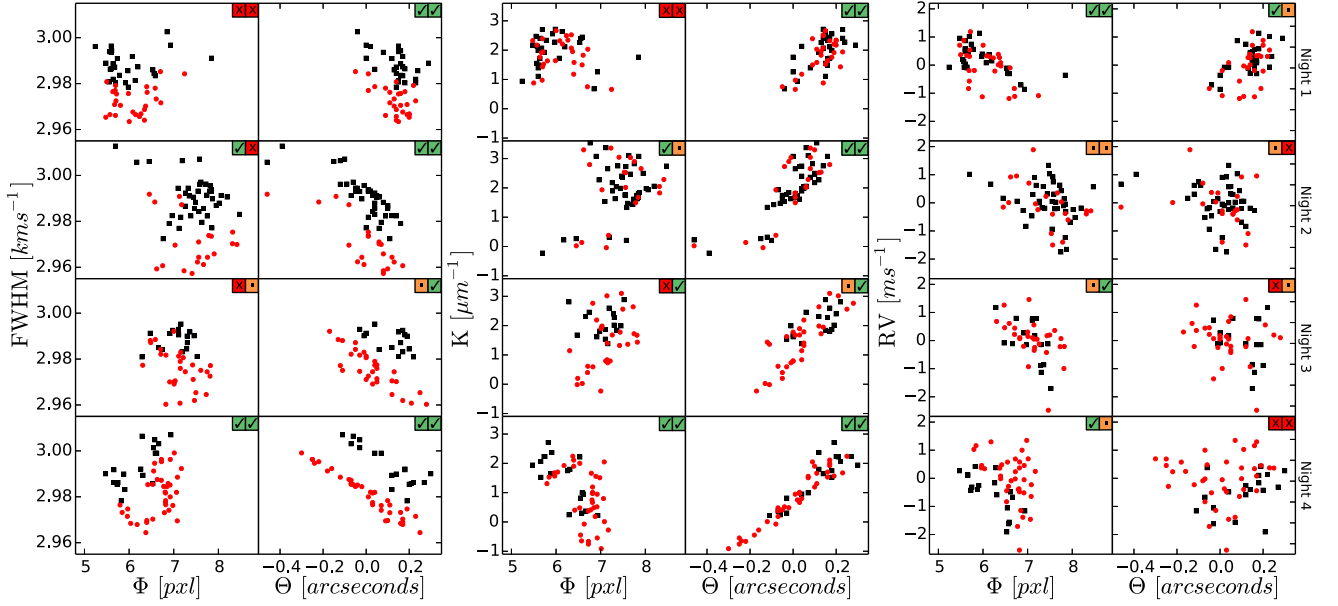


**Figure 8.** Correlation of the spectroscopic indices, FWHM (left-hand panel),  $K$  (central panel) and RV (right-hand panel), with the image indices,  $\Phi$  and  $\Theta$ . Each row matches one night. Black squares correspond to GJ 725A and red dots to GJ 725B. Two squares in the top-right corners of each plot indicate the FAP for GJ 725A and B, respectively; from the left: ticked green squares means FAP < 1 per cent, dotted orange 1 per cent  $\leq$  FAP < 10 per cent and crossed red FAP  $\geq$  10 per cent. Main correlations are as follows: FWHM– $\Theta$ ,  $K$ – $\Theta$  and RV– $\Phi$ . GJ 725B RVs are residuals to the Doppler signal discussed in Section 4.5.

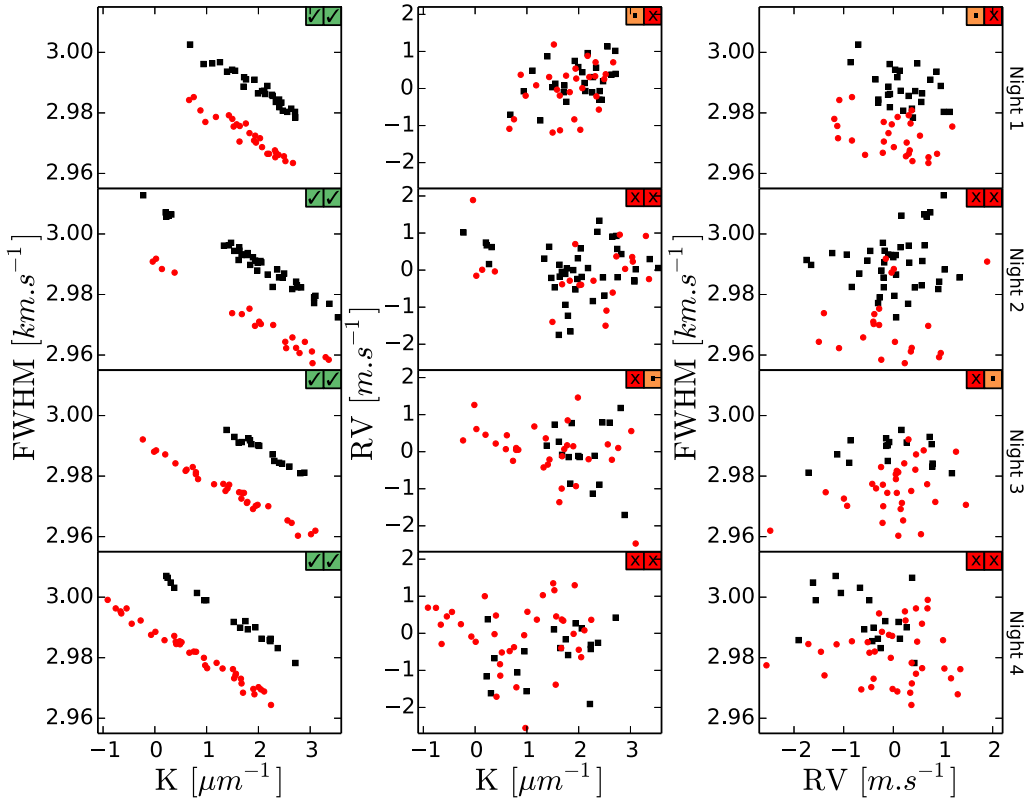


**Figure 9.** Best correlation linear models fitted for the spectroscopic indices: FWHM– $K$  (left-hand panel), RV– $K$  (central panel) and FWHM–RV (right-hand panel). Markers and top-right corner squares are coded as in Fig. 8. Among these indices FWHM– $K$  was the only correlation detected.

#### 4.2 Independent measurements and validation experiments

Systematic variability in the measurements can be caused by *intrinsic* changes in the line profile (i.e. instrumental), by sub-optimal procedures in the measurement of these quantities (i.e. algorithmic), or both. For example, even if the line profile is perfectly stable, inaccuracies in the fitting of the flux or background subtraction will produce apparent variability of measurements of the line shape. In particular, the cross-correlation profiles are obtained by

mic), or both. For example, even if the line profile is perfectly stable, inaccuracies in the fitting of the flux or background subtraction will produce apparent variability of measurements of the line shape. In particular, the cross-correlation profiles are obtained by



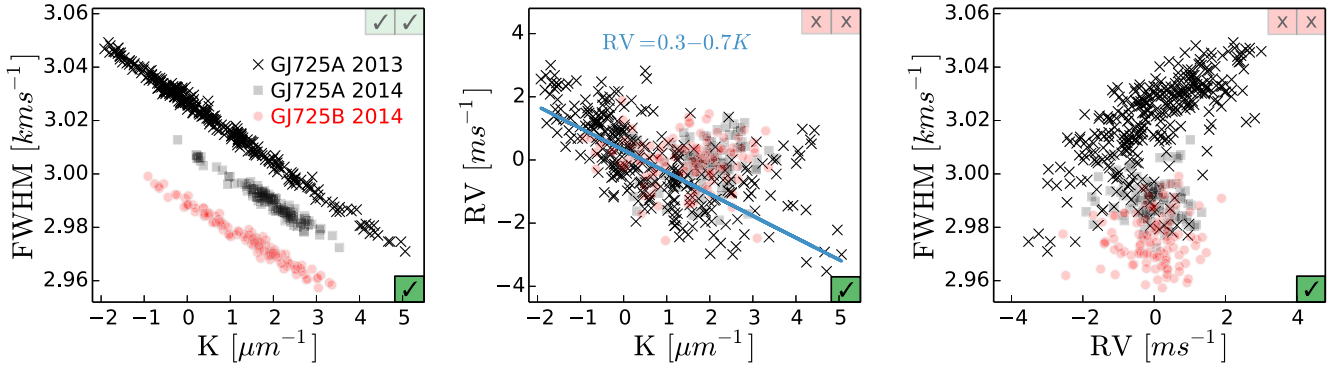


**Figure 10.** Spectral indices correlations for the five consecutive high-cadence nights of GJ 725A observed in 2013 August (black crosses). Alternating run observations taken in 2014 are also shown for comparison. The FAP is coded as in Fig. 8 where the low-right square refers to the 2013 data. The wider range of AM sampled in 2013 might have uncovered a chromatic effect also in the RVs (centre). Blue line and equation correspond to the tentative linear fit we applied to correct the RV data (see Section 4.3). On the left plot, the negative slope of the 2013 FWHM– $K$  correlation is compatible with the 2014 results, pointing out towards an instrumental (or software) common origin. The FWHM–RV is shown in the right-hand panel.

computing some weighted mean of the profiles of the individual spectral orders. Because the effective line profile of each individual order is different, changes in the weights (e.g. if the weights are computed using Poisson statistics from the photon counts) will produce spurious variability correlated with these changes. In other words, a different SED implies a different local SNR for each order. On the other hand, an inaccurate continuum or background subtraction will cause different mean line profiles at each spectral order. As a result, we can obtain a modified final mean line profile when we combine a variable weight distribution with different profiles at each order. Furthermore, the RV and FWHM values obtained from the final profile will be also different with the SED. Thus, if our methods do not perform a good continuum or background subtraction, we can measure spurious RV or FWHM variabilities even when the instrument is stable.

Such an effect was earlier reported by Bourrier & Hébrard (2014) on 55 Cancri. Following their findings, the DRS flux-normalizes the continuum of all the spectra with respect to a reference spectrum for F, G and K stars. However this has not been yet implemented for M stars, because, as it was defined, some zero division problems can occur in the bluer part of the spectra (Pepe, private communication).

In order to validate if the algorithms we used could be the cause of the observed variability in the measurements, we have performed the two experiments detailed below.

#### 4.2.1 Experiment 1: RV measurement against pSED variability

HARPS-TERRA fits the flux iteratively. It carries out a least-squares fit to minimize the difference between the observations and a template (built from the observations). In particular, the magnitude to minimize,  $R$ , is given by

$$R(\lambda) = T[\alpha_v \lambda] - f[\lambda] \text{FN}, \quad (3)$$

$$\text{FN} = \sum_{m=0}^M \alpha_m (\lambda - \lambda_c)^m, \quad (4)$$

where  $T$  is the template,  $f$  is the observed spectra and FN the flux normalization term. Thus, HARPS-TERRA fits simultaneously the Doppler shift ( $\alpha_v$ ) and the others parameters which account for the shape of the continuum ( $\alpha_m$ ) at each order ( $m$ ). As a consequence, the  $\alpha_m$  parameters are also modelling instrumental flux variations effects such as the atmospheric differential refraction or tracking errors.

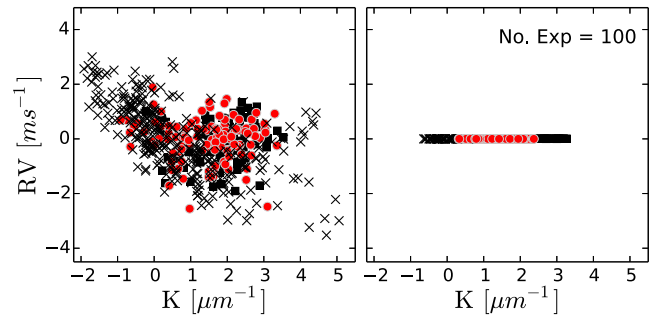


**Figure 11.** RVs plotted versus the  $K$ -index when the input corresponds to the real observations (left plot) or to a set of 100 flux-distorted spectra calculated from an observed epoch (right plot). HARPS-TERRA measures relative values and centres the RV at  $0 \text{ m s}^{-1}$ . The zero-values (rms below  $2 \times 10^{-6} \text{ m s}^{-1}$ ) on the right plot indicate that the normalization carried out by HARPS-TERRA ensures RVs independent on the flux distortions included deliberately to perform this experiment.

In order to validate if this simultaneous continuum fitting technique applied by HARPS-TERRA prevents the RVs from being affected by chromatic correlations, we performed the experiment detailed below.

We selected three epochs, one for each star and run, and we changed the flux of their spectra as

$$f_{\text{new}}(\lambda, t) = f_{\text{orig}}[\lambda, t] [1 + S(t) * (\lambda - \lambda_{\text{cR}})], \quad (5)$$

where  $S(t)$  randomly takes values between 0 and  $2.086 \mu\text{m}^{-1}$ . This range was selected to ensure positive new fluxes at least for the last 31 orders that were used in the second experiment (detailed in Section 4.2.2), and to result in flux distortions below 20 per cent (approximately the SED distortion measured in the linear range used to calculate  $K$ ). We repeated this calculation several times, and, in total, we obtained 100 new synthetic spectra for each of the three selected epochs. Afterwards, we post-processed these synthetic spectra with HARPS-TERRA, recovering in all cases an RV with rms below  $2 \times 10^{-6} \text{ m s}^{-1}$  for the three epochs (see Fig. 11).

This result indicates that the RVs measured with this template-matching algorithm are mostly insensitive to changes in the SED. HARPS-TERRA is properly fitting the flux of the spectra, and thus, our intentionally introduced wavelength distortions cannot be the cause of the observed RVs variability (neither of the RV– $K$  correlation).

#### 4.2.2 Experiment 2: line profile width against pSED variability

HARPS-TERRA provides an independent measurement of the RV, but we do not have any equivalent for the FWHM. With the aim of checking if the strongest FWHM– $K$  correlation could be due to a software issue related with the weighting of the orders (see detailed explanation at the beginning of this section), we estimated the profiles using an independent LSD technique (Donati et al. 1997). In particular, we used the implementation given by Barnes et al. (1998, 2012).

The least-squares routine involves solving the mean-line profile which, when optimally convolved with a line list, gives the best match to the observed spectrum. Generally, the line list used is just a theoretical identification of wavelengths and depths. Instead, we used the high SNR template computed by HARPS-TERRA to obtain a more realistic empirically determined list of lines. This template is built by co-adding all the observed two-dimensional spectra given by the DRS (the so-called e2ds). Those regions of the spectrum with strong telluric absorption or strong stellar molecular bands were not used for the deconvolution.

Like the DRS, the LSD discards some wavelengths in the blue part of the spectra (only those corresponding to the last 31 orders were used, while the DRS uses the reddest 51 orders). However, in contrast to the DRS, the LSD does not calculate one profile per order. The deconvolution is performed on each spectrum using all lines (including those repeated in adjacent orders) to obtain one single LSD profile per exposure. Our LSD method normalizes each spectrum to a template to obtain an individual continuum. That is, each spectrum in turn is divided by the template spectrum and a cubic order polynomial is fitted to the residuals. Later, the continuum of each spectrum is obtained by multiplying this cubic polynomial fit by the template continuum, which was previously obtained by iteratively fitting a fifth degree polynomial to the template. Because each spectrum is normalized to an individual continuum, we did not expect variability related with weighting problems arising from the algorithm or background issues (see beginning of this section).

The output of the LSD technique is a mean line profile in absorption. These  $F_i(t)$  profiles can be inverted (sign changed) after we have subtracted their residual continuum  $w(t)$ , producing a normalized (positively defined) probability distribution function  $f(t)$ . Then, the moments of  $f(t)$  can then be computed as

$$f_i(t) = w(t) - F_i(t) \quad (6)$$

$$\hat{M}_n(t) = \frac{\sum_{i=1}^N [f_i(t)] v^n}{\sum_{i=1}^N f_i(t)}. \quad (7)$$

Before calculating the moments with equation (7), we truncated the profiles in a range of  $\pm 20 \text{ km s}^{-1}$  around the estimated zero-velocity (the velocity of the co-added barycentric corrected high SNR template from which we obtained the line list applied during the deconvolution process), and we excluded the negative values resulting after the continuum inversion. This truncation was done to avoid including wing distortions in the moments calculation. The profiles were calculated with a mean velocity increment of  $0.81 \text{ km s}^{-1}$  – value that corresponds to the pixel size of the HARPS-N detector – and later interpolated by a factor 10 using a spline function. The order zero moment,  $M_0$ , corresponds to the integral of the normalized profile.  $M_1$  is equivalent to its centroid (all spectra are aligned to zero-velocity before computation of the LSD profile) and  $M_2$  corresponds to the profile variance and thus, as the FWHM, is a measurement of the width of the line profile.

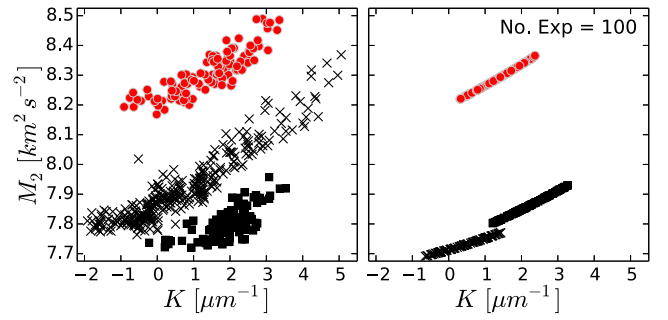


**Figure 12.** Moment of second order ( $M_2$ ) of the LSD profiles versus the  $K$ -index for the observed (left plot), and for the synthetic (right plot) spectra. The trend for the synthetic data reproduces the observations pointing out a software issue.

With the aim of testing the LSD performance, we calculated the LSD profiles of the flux modified spectra that we used in the previous section to test the software HARPS-TERRA; i.e. we took the same three spectra (one for each star and run) and we modified their flux following the equation (5). In this case, the second-order moment (or  $M_2$ ) calculated from these contaminated profiles, correlated with  $K$  in a way analogous to the observations (see Fig. 12). This implies that, even with our method that fits the continuum of each spectrum individually, we find a strong correlation of the measurement of the line width (through  $M_2$ ) with the artificially introduced slope of the pSED. In other words, the changes in the distribution of the flux along the CCD can drive the FWHM variability. Then, the largest correlation involving the FWHM– $K$  relation can be explained as an inaccurate computation of the profile by the algorithms. Neither the DRS nor the LSD method produce accurate enough measurements. Actually, the fact that we need to correct a residual continuum  $w(t)$  for each deconvolution profile may arise from a non-perfect description of the continuum.

According to our experiment, only the RV measurements obtained by the HARPS-TERRA algorithm, seem to be insensitive to the SED variability. This result indicates that new algorithms that simultaneously fit for the continuum of each echelle order and the line profile need to be developed, or the current methods refined to account for this.

To use the FWHM index produced with the M-dwarf mask of HARPS-N, one should – at the very least – apply some decorrelation procedure. Otherwise, all this index is tracing are small changes in the measured SED produced by the expected flux losses on fibre-fed spectrographs.

#### 4.3 Detrending strategies for archival FWHM and RV obtained with HARPS

Once we clarified that the strongest FWHM– $K$  correlation has an algorithm origin, we aimed at defining an empirical function to detrend the FWHM time series from chromatic effects. The function should be valid for (at least) the GJ 725A+B pair and other stars with similar spectral types (note that the chromatic nature of the effect will likely affect different spectral types differently). We made use of both, 2013 and 2014 data, to compute the detrending law.

The FWHM contains additional contributions from other effects. In particular, since the observations span over a finite amount of time, the FWHM will be broadened by the change in the barycentric velocity of the observer. The following procedure was designed to remove the effect of this barycentric broadening (which can account

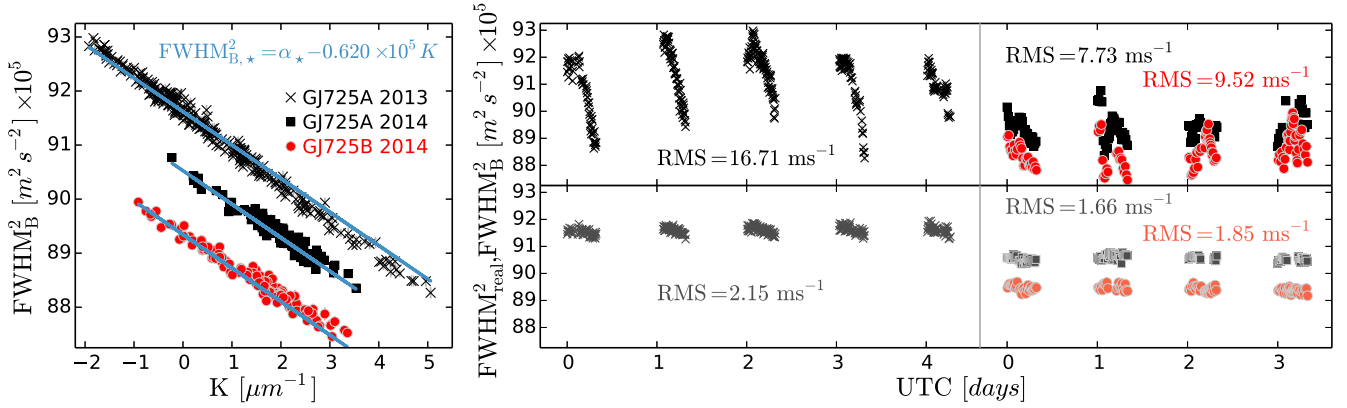


**Figure 13.** Left-hand panel: FWHM (barycentric corrected) and  $K$ -index correlation. Black squares and red dots match GJ 725A and B, respectively. Blue lines and equation correspond to the best-fitting function. We want to emphasize that the empirical law is unique. Note that the chromatic correction consists of detrending the data by subtracting the slope term. Right-hand panel: time series before ( $\text{FWHM}_B^2$ , top) and after ( $\text{FWHM}_{\text{real}}^2$ , bottom) the chromatic correction. The FWHM is flattened and corrected from chromatic distortions caused by the atmosphere. The rms is reduced by a factor of 8 in 2013 and by a factor of 5 in 2014.

for several  $\text{m s}^{-1}$  depending on integration time and coordinates of the star).

The central moments of a distribution can be denoted as  $M_k = \langle (x_i - \bar{x})^k \rangle$ . Thus,  $M_2 = \text{Var}(x)$ , the variance of the distribution which, for two independent distributions, satisfies the additive property:  $\text{Var}(x + y) = \text{Var}(x) + \text{Var}(y)$  (Press 1992). The mean line profiles of the spectral orders can be considered as a probability density function. In consequence, the FWHM should also be a variance.

The observed  $\text{FWHM}_{\text{obs}}^2$  is the sum of three terms:

$$\text{FWHM}_{\text{obs}}^2 = \text{FWHM}_{\text{real}}^2 + B^2 + I^2, \quad (8)$$

where  $\text{FWHM}_{\text{real}}$  is the true line profile we want to measure, and  $B$  and  $I$  are as follows –

(i) The barycentric correction ( $B$ ): it is a squared velocity value we have to subtract to the square of the observed FWHM to correct it from the movement of Earth on its orbit. To first order, let us assume that the velocity  $v$  of the observer changes between the initial instant  $t_i$  and the end-of-integration time  $t_f$  by  $dV$ . The effect of the barycentric broadening is then a convolution of the stellar profile with the double of the variance of a boxcar distribution ( $F(v)$ ) of width  $dV$ :

$$B^2 = 2 \int_{-\infty}^{\infty} F(v) v^2 dv = 2 \frac{dV^2}{12}, \quad (9)$$

where,  $C$  being a constant,  $F(v)$  is the boxcar function  $f(v)$  normalized to have unit area as follows:

$$F(v) = \frac{1}{C dV} f(v), \quad (10)$$

$$f(v) = \begin{cases} C & \text{if } \frac{-dV}{2} < v < \frac{dV}{2} \\ 0 & \text{if } v < \frac{-dV}{2} \text{ or } v > \frac{dV}{2} \end{cases} \quad (11)$$

This correction can be exactly computed using the observation, the exposure time and a custom-made code used to compute the barycentric correction (implemented within the HARPS-TERRA software).

(ii) Chromatic effect correction ( $I$ ): this term contains the correlation with the chromatic  $K$ -index as computed in previous sections. We searched for the linear model which best fitted the observed

FWHM corrected from barycentric term ( $\text{FWHM}_B$ ), and the  $K$ -index series,

$$\text{FWHM}_B^2 = \text{FWHM}_{\text{obs}}^2 - B^2 = \alpha + \beta K, \quad (12)$$

where  $\alpha$ , the offset, is a nuisance parameter, which is equal to  $(90.53 \pm 0.02) \times 10^5 \text{ m}^2 \text{s}^{-2}$  for GJ 725A,  $(89.34 \pm 0.01) \times 10^5 \text{ m}^2 \text{s}^{-2}$  for GJ 725B, and to  $(91.620 \pm 0.004) \times 10^5 \text{ m}^2 \text{s}^{-2}$  for GJ 725A observed in 2013.

Thus, we defined the chromatic correction term as

$$I^2 = \beta K, \quad (13)$$

where  $\beta = (-0.620 \pm 0.003) \times 10^5 \text{ m}^2 \text{s}^{-2} \mu\text{m}$  is the average of the values obtained for the three data sets independently. The low degree of scatter in the values (coefficient of variation lower than 10 per cent) means that the average is representative and, thus, we can define a common law which is the same for both stars and all observed nights (see Fig. 13, left-hand panel).

Finally, the FWHM corrected from barycentric and chromatic effects can be written as

$$\text{FWHM}_{\text{real}}^2 = \text{FWHM}^2 - 2 \frac{dV^2}{12} - \beta K, \quad (14)$$

and its error, obtained by applying simple error propagation functions, as

$$\sigma_{\text{FWHM}_{\text{real}}^2} = \sqrt{4 \text{FWHM}^2 \sigma_{\text{FWHM}}^2 + K^2 \sigma_{\beta}^2}. \quad (15)$$

Results are shown in Fig. 13. The same slope for 2013 and 2014 data was expected as it is caused by the same instrumental effect. However, results indicated some systematic residual effects, especially in the 2013 data. This extra variability might be related to some lesser degree contributions specific to each run. However, as the main correlation might have the same origin, we still prefer to apply the same empirical law to detrend all the data sets. We also expected the zero-point offset ( $\alpha$ ) of the two runs to be the same for GJ 725A, but the change could be due to an instrument focus readjustment carried out between the two observational campaigns. In spite of these discrepancies, the improvement is obvious, the rms is reduced a factor of 5: GJ 725A from 7.73 to 1.66  $\text{m s}^{-1}$ , GJ 725B from 9.52 down to 1.85  $\text{m s}^{-1}$ ; and 87 per cent for the 2013 run in GJ 725A, from 16.71 down to 2.15  $\text{m s}^{-1}$ . We want to point out that

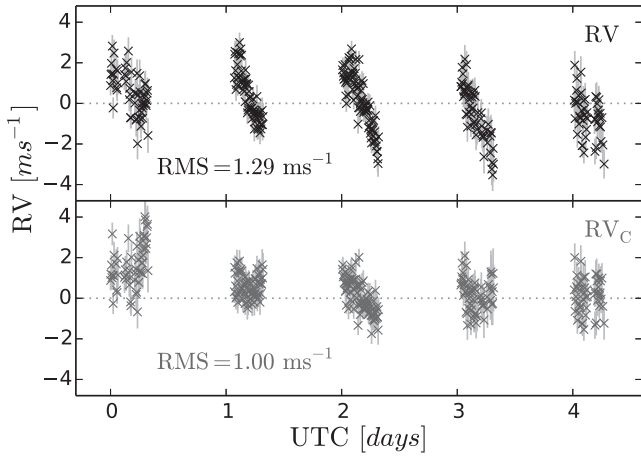


**Figure 14.** 2013 RV time series of GJ 725A before (top panel) and after (bottom panel) applying the empirical function to detrend the RV- $K$  correlation. The rms decreases by a factor of 1.3.

the reduction of rms comes from the presence of highly structured noise, which makes the new time series of the FWHM a much more reliable tracer of the physics occurring in the photosphere of the star.

On the other hand, the intranight systematic in the RVs can be also modelled with a linear function. Bourrier & Hébrard (2014) detected similar RV correlation for the 55 Cnc high-cadence data observed with HARPS-N. They used the ratio of SNR of two orders as the detrending quantity, which is a simpler version of our chromatic  $K$ -index. As discussed before, we did not find any significant correlation for the 2014 run. Therefore, we have only detrended the 2013 data, as following:

$$RV_C = RV - \omega K, \quad (16)$$

where  $\omega = -0.7 \pm 0.2 \text{ m s}^{-1} \mu\text{m}^{-1}$ . This value of  $\omega$  is obtained by fitting the linear correlation law to each night independently to avoid contamination by additional, longer term variability (e.g. planets or induced activity happening at time-scales of a few days). Finally, the fitting parameters (see equation in the central panel of Fig. 9) are the weighted mean of the  $i$ th values.

Detrended RVs, shown in the bottom panel of Fig. 14, have a mean peak-to-peak difference of  $3.3 \text{ m s}^{-1}$ . The rms is reduced from 1.29 down to  $1.00 \text{ m s}^{-1}$ , which is close to the photon noise of the HARPS-N observations.

We advise caution in using the correlation laws defined here to detrend the FWHM and RVs from HARPS-N observations. As we have seen, instrumental updates and (possibly) spectral types might produce slightly different values for the correlation laws. As a general rule, in the case of aiming at detrending archival data, first we strongly recommend to compute the chromatic  $K$ -index, and secondly, verify if there are chromatic effects; that is, verify if there are correlations between the  $K$ -index and the main data-products (e.g. RVs, FWHM or other indices). Finally, in the case of detecting significant correlations, follow the detrending steps explained in this study. We want to note that, in the case of detecting correlations with the RVs, it is preferable to include  $K$  as a correlation term in the model used to search for Keplerian signals instead of applying pre-whitening like methods (see an example in Anglada-Escudé et al. 2014).

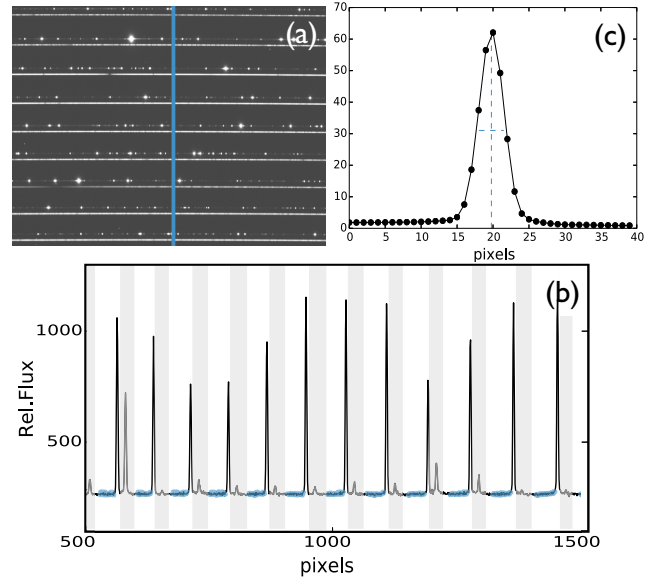


**Figure 15.** Layout of the cross-dispersed profile calculation process. To extract the cross-dispersed profiles (B), the raw images are cut in the spatial axis following the direction of the blue line (A). Simultaneously with the science observations, we recorded emission lines from a ThAr lamp (see bright spots in the raw image). We blocked the lamp lines (B, shaded areas) before selecting the points used to fit and subtract the floor level (B, blue dots). Finally, after normalizing each peak to its maximum, we cross-correlated the profile with the flat raw image to obtain a mean line profile of the column (C).

#### 4.4 Cross-dispersion profiles

The cross-dispersion profile, or the mean profile obtained from making a cut of the échelle spectrum across the orders, is very sensitive to illumination distortions produced at the fibre entrance such as changes of the telescope focus, seeing increases or pointing errors. The reason for this is that each cut across the order is a section of the fibre image; in fact the fibre size defines the width of the order. Therefore, the cross-dispersion profile is by itself a measure of the instrumental profile and can be used to measure the illumination stability in the detector. For example, if the wavelength dependence variations of the flux of the spectra were due to a non-perfect smoothness of the instrumental profile (i.e. due to an inefficient fibre scrambling system on HARPS-N; Avila et al. 2004), we would expect to find a correlation between the width of the cross-dispersion profile and the  $K$ -index.

To measure this profile, we cut the raw images across the cross-dispersed axis, extracting in that way the flux at each column of the reddest half of the CCD (see diagram in Fig. 15). After blocking the lamp emission, which is recorded in the science image simultaneously using a secondary fibre, we fitted and subtracted the floor level using a polynomial. The counts obtained in between consecutive science orders were compatible with the bias level obtained during the standard calibration performed at the beginning of the night. However, we fitted a polynomial instead of subtracting a constant bias level to better account for other possible background effects that can introduce biases in the final width of the cross-dispersion profile. Then, we normalized each order to its maximum and we cross-correlated each column of the raw image with the corresponding flat column. After that, we fitted a Gaussian to this



cross-correlated profile, calculating the cross-dispersed FWHM at each column as

$$\text{FWHM} = 2\sigma \sqrt{2 \log 2}, \quad (17)$$

where  $\sigma$  corresponds to the width of the fitted Gaussian. We note that this function includes a fourth parameter (an offset) in an attempt to model the background flux variabilities.

Because the detector is flat, the image of the fibre on to the detector – and thus the FWHM in the cross-dispersed direction – increases towards the detector edges. To avoid this effect, we took the differential cross-dispersed FWHM measurements of each column with respect to the first epoch. Furthermore, the detector edges are more sensitive to illumination changes (see table 7 of the HARPS-N User Manual),<sup>4</sup> and this causes the measurements at the edge columns to be more sensitive to SNR variabilities. Aiming at correcting the SNR dependences of this origin, we detrended the cross-dispersed FWHM using the fitted offset parameter from the Gaussian model. The final measurement for each exposure (FWHM<sub>cd</sub>) was obtained as the median along the column detrended values.

We have also calculated the centroids in the cross-dispersed axis. This measurement corresponds to the mean parameter of the Gaussian function fitted to the profile. The cross-dispersed centroid (or CEN<sub>cd</sub>) of the exposure was directly defined as the median of all the column values. In this case, we could not use the background level to detrend this measurements because, as it was expected, the centroid of the Gaussian did not move with changes of the background flux level; as a consequence we still had some correlation of the CEN<sub>cd</sub> with the SNR.

In spite of the corrections explained above, we detected the FWHM<sub>cd</sub> to be more dispersed at low SNRs. Therefore, we performed an additional experiment to discard possible non-linearity effects of the detector as a source of variability. We let the values of the cross-correlated profiles of the 20 per cent of the exposures with worse SNR to randomly vary  $\pm 0.2$  per cent, total amount that could be associated with a non-linearity effect.<sup>5</sup> However, we found no significant changes, discarding the non-linearity as responsible for any change in the FWHM<sub>cd</sub>.

If the spectral FWHM variability was due to illumination effects (instead of being a pure software issue), the variation of the cross-dispersed FWHM with  $K$  would be significant. However, as we show in Fig. 16, the scatter of the FWHM<sub>cd</sub> is below 1 mpxl (1 mpxl  $\sim 0.8 \text{ m s}^{-1}$ ). Moreover, we did not detect any significant correlation with  $K$ . The cross-dispersed centroids, whose maximum rms was only  $0.8 \text{ m s}^{-1}$ , do not correlate with  $K$  either, opposite to what we detected for its spectral counterpart in the 2013 observations.

In consequence, we do not detect significant distortions of the image on to the detector through the measurements in the cross-dispersed direction. Bearing in mind that, in the case of the CEN<sub>cd</sub> we still deal with some correlation with the SNR, this result indicates that, neither the large variability detected on the spectral FWHM nor the RV– $K$  correlation measured for the 2013 data, are due to a non-perfect smoothness of the inhomogeneities of the injected light spot. This result validates the use of the cross-dispersed profiles as a useful test to account for illumination issues.

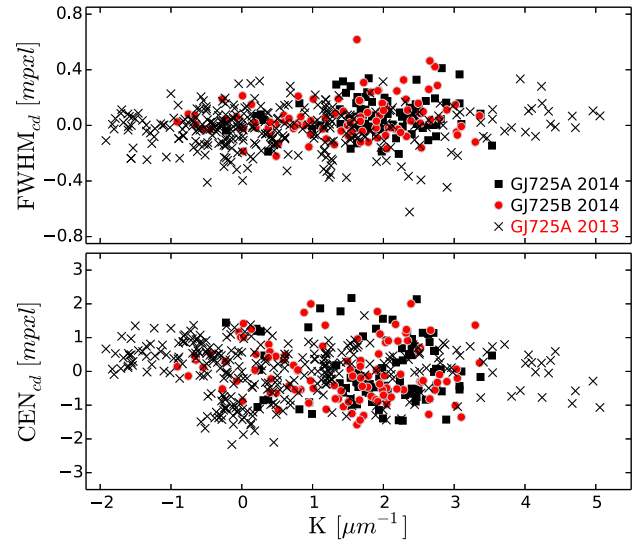


**Figure 16.** FWHM (upper panel) and centroids (lower panel) fitted to the mean line profile calculated on the cross-dispersed direction (perpendicular to the spectral axis). No significant correlation with the  $K$ -index was measured, ruling out a scrambling issue. The FWHM<sub>cd</sub> values are referred to the first exposure of the series. The average values of the three CEN<sub>cd</sub> series were subtracted to better compare its scattering.

#### 4.5 Possible GJ 725B planet candidate?

In this section we discuss a possible planet hosted by GJ 725B. As we pointed out in Fig. 6, the F-ratio excess detected in the RV differential periodogram could be compatible with a planet orbiting either GJ 725B or GJ 725A.

To assess the significance of the variability and its possible fit to a Keplerian orbit, we use likelihood periodograms as described in Baluev (2009) and in Anglada-Escudé et al. (2013). The model

$$v_r(t) = \gamma + A \cos\left(\frac{2\pi}{P} \Delta t\right) + B \sin\left(\frac{2\pi}{P} \Delta t\right), \quad (18)$$

includes two sinusoids (two parameters,  $A$  and  $B$ ) plus velocity offset (+1 parameter,  $\gamma$ ). We used this circular model after having obtained an eccentricity compatible with zero with the complete Keplerian model. Like in classic periodograms, the likelihood periodograms produce a map of peaks for each of the investigated periods. However, in this case the power of the peaks is defined by the model that maximizes the logarithmic of the likelihood statistic ( $\ln \mathcal{L}$ ). The  $\ln \mathcal{L}$  maximization and  $\chi^2$  minimization are equivalent, but the likelihood method has the advantage, with respect to traditional periodograms, of including the so-called jitter as a free parameter (excess white-noise, +1 parameter). Using the likelihood statistic has a further advantage:  $\ln \mathcal{L}$  gives a probability, and the ratio of likelihoods  $\Delta \ln \mathcal{L} = \mathcal{L}_{\text{null}} - \mathcal{L}_{\text{model}}$  directly estimates the relative probabilities between models. Properties of the likelihood periodograms are described in full detail in Baluev (2009, 2012).

The likelihood periodogram analysis associates the peak detected in the RVs differential periodogram with a  $2.7 \pm 0.3$  d signal with an amplitude of  $1.2 \text{ m s}^{-1}$ . This means that a model of a sinusoid at that period has a  $\Delta \ln \mathcal{L} = 32.79$  when compared with a model with no signal. This corresponds to an FAP  $< 1.5 \times 10^{-11}$ , which is much smaller than the usual 1 per cent threshold. A compatible period is obtained when analysing GJ 725B RVs independently, indicating that the variability comes from this star. Besides the common

<sup>4</sup> <http://www.tng.iac.es/instruments/harps/>

<sup>5</sup> See the ESO report about the EEV44-82 CCDs at <https://www.eso.org/sci/facilities/develop/detectors/optdet/docs/reports/EEV-report.html>



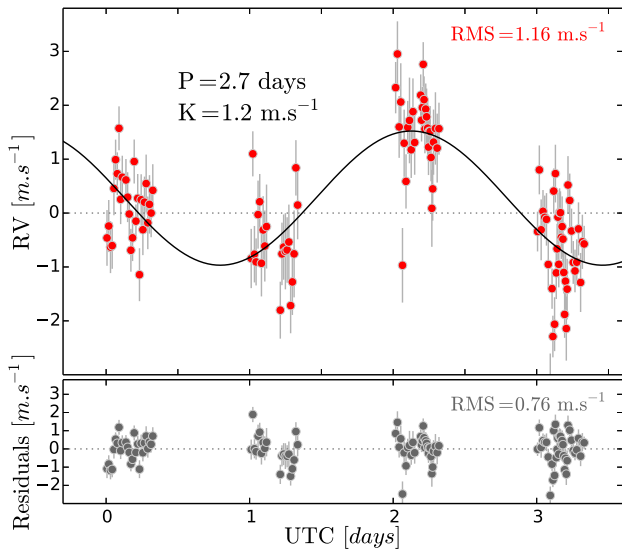


**Figure 17.** GJ 725B planet candidate signal. Red dots in the top panel are the GJ 725B RVs for the 2014 run. The black line is the circular Keplerian model best-fitting the data ( $P = 2.7$  d,  $K = 1.2$  m s $^{-1}$ , FAP < 0.1 per cent and  $\Delta \ln \mathcal{L} = 49.13$ ). Residuals to this model are plotted in the lower panel. The rms decreases from 1.16 to 0.76 m s $^{-1}$  on the residuals. Time is referenced to the first exposure of the run.

variability in both stars, no additional significant RV variability is detected on GJ 725A.

The variability in GJ 725B is consistent with a  $1.2 M_{\oplus}$  planet with an orbital period of  $2.7 \pm 0.3$  d period (or 0.025 au, see Fig. 17). While the statistical significance is very high (a sinusoidal model is massively preferred over no signal at all), its nature cannot be confirmed because we cannot verify its strict periodicity. Doppler follow-up observations and/or transit searches will be needed to confirm it.

## 5 DISCUSSION AND CONCLUSIONS

We obtained high-cadence observations using the HARPS-N spectrograph on the nearby M-dwarf binary system GJ 725A+B. The two stars alternating observations unveiled common strong systematic effects in the measurements of the width of the mean line profile (through the FWHM), and also in the RV measurements to a lesser degree. The presence of these systematic effects is a likely component of the floor noise observed in long-term Doppler programmes of M-dwarf stars, and seriously affects the use of high-cadence observations for very low amplitude signal searches ( $< 2$  m s $^{-1}$ ).

The systematic effects seem to be related to flux losses due to imperfect corrections of chromatic effects introduced by the Earth's atmosphere at the telescope-fibre interface. This suspicion is motivated by several measurements and correlations observed in pre-fibre images of the star compared to a number of measurements on the spectrum, most notably changes in the slope of the measured SED. The comparison of measurements between the two stars (and their almost identical systematic behaviour) shows beyond reasonable doubt that the significant variability observed with high cadence on M dwarfs has an instrumental origin. While most variability in the width of the line profile is likely to be caused by the algorithms used, smaller residual RV variability remains unexplained.

HARPS-N includes an ADC which corrects the atmospheric dispersion; however, other sources of error such as the atmospheric extinction or the wavelength dependence with the seeing remain uncorrected. A direct consequence of a non-optimal correction of the Earth's atmosphere is a superposition of wavelength-dispersed images of the star at the fibre entrance. This causes the light injected into the fibre to vary in wavelength as the energy peak (used for centring the image in the fibre during exposure) changes with the airmass. To measure whether this was causing distortions in the spectra, we defined the  $K$ -index, which measures how the flux is distributed across the detector during the observations (i.e. accounts for the SED variability). Besides, we measured variability of the  $K$ -index. This, as well as with the airmass, resulted to be correlated with the distortions on the pre-fibre images. However, while these SED variabilities cause changes in the flux, this does not necessarily imply that the instrumental profile shape changes too (neither the data-products) due to illumination effects. In fact, to avoid illumination dependences, all current high-resolution fibre-fed spectrographs apply scrambling methods (Avila et al. 2004). Therefore, a correlation of the SED variability with the data-products is not expected. Nevertheless, we found a strong correlation of the SED variability with the line width (through the FWHM) and a correlation with the RVs only for our 2013 single star run on GJ 725A. Further measurements of the spectral order shapes in the cross-dispersed direction ruled out an inefficient scrambling as the origin for these correlations. These measurements also validate the use of the cross-dispersed profiles as a useful test to account for illumination issues on other echelle spectrographs.

We performed a couple of tests to validate the algorithms used in this work. Results indicate that, whereas HARPS-TERRA properly corrects and models the continuum, the DRS is sensitive to changes in the slope of the SED. This computational issue explains the strong FWHM- $K$  correlation; however, 2013 RV- $K$  correlation remains unexplained and has to be caused by another effect. Since the width of the mean line profile is a parameter very sensitive to magnetic activity events (e.g. Reiners et al. 2013), the FWHM is often used as an activity indicator and a tool to decorrelate Doppler time series. Thus, there is a value in detrending this index. We outline a procedure to decorrelate the HARPS-N FWHM measurements using the slope of the SED. A tentative decorrelation law is also proposed for the 2013 RVs. The decorrelation laws are likely to be slightly different on each target (especially for targets of different spectral types), so we advise to obtain the SED slopes changes with the  $K$ -index and perform similar verifications on all individual targets of a given programme.

Ideally, new algorithms that simultaneously fit for the continuum and the line profile need to be developed to account for the FWHM variability. Other option is to refine the current methods, as it was already done in the last DRS version for F, G and K stars, where the continuum is renormalized with respect to a reference spectrum. Regarding the variability of the RVs in the 2013 single run in GJ 725A, given the large correlation with the airmass and the erroneous updating of the ADC movement pointed out during other campaigns, we suspect that the most likely explanation for it was the sub-optimal performance of the atmospheric correction. The possibility of a systematic ADC failure only during continuous mode observations (where the pointing procedure is not redone between same object exposures) was ruled out by the HARPS-N core team (Cosentino, private communication). However, our *in situ* monitoring of the ADC parameters during posterior HARPS-N campaigns showed that, under some unknown circumstances, the ADC values

seem no to be updated. Therefore, we suspect that the ADC failed during this 2013 run.

Remaining correlations with the image distortions might be the origin for the noise floor level which popped up as common signals in the GJ 725A+B alternating run. As a by-product, we have shown that the GJ 725A+B pair is stable enough to be used as a benchmark case for commissioning of future high-precision spectrographs, at least down to  $\sim 1\text{--}2\text{ m s}^{-1}$ . Indeed, CARMENES spectrograph (Quirrenbach et al. 2014) is planning to use this system for validation purposes. The  $\sim 1\text{--}2\text{ m s}^{-1}$  limit is possibly set by a low-mass companion orbiting GJ 725B, whose presence will be further investigated in future campaigns.

Long-term surveys [like the HARPS Guaranteed Time Observations (HARPS-GTO)], try to observe all the stars at the same airmass each night, minimizing sources effects related to airmass and scrambling, and randomizing possible systematic shifts occurring within a night. However, this is not possible for programmes which require continuous high-cadence observations. Many science cases, such as the molecule detection on transiting exoplanets (Snellen et al. 2010; Martins et al. 2013), can benefit from an extremely stabilized instrumental profile and robust procedures to measure it. Concerning Doppler spectroscopy, we note that an extra effort should be put into the image stabilization and correction of chromatic effects such as those reported here ( $\sim 1\text{ m s}^{-1}$ ) in order to clean spurious signals and get the most of the new technologies for wavelength calibration at  $\text{cm s}^{-1}$  levels, like laser frequency combs (Probst et al. 2014). The best wavelength determination is useless if systematic signals populate the periodograms.

## ACKNOWLEDGEMENTS

The authors thank E. Sánchez Blanco, M. C. Cárdenas Vázquez, N. Piskunov, F. Pepe, C. Lovis, R. Cosentino, X. Dumusque, D. Staab and C. Haswell for constructive comments and discussions. They also acknowledge funding from AYA2011-30147-C03-01 by MINECO/Spain, FEDER funds/EU, and 2011-FQM-7363 of Junta de Andalucía/Spain (ZMB, PJA and CR-L); ZMB acknowledges support from the UGR/Spain and financial funding from FPI BES-2011-049647 of MINECO/Spain. This study is based on observations made with the Italian Telescopio Nazionale Galileo (TNG) operated on the island of La Palma by the Fundación Galileo Galilei of the INAF (Istituto Nazionale di Astrofisica) at the Spanish Observatorio del Roque de los Muchachos of the Instituto de Astrofísica de Canarias. The authors thank the referee T. Böhm for his suggestions that helped improved this paper.

## REFERENCES

- Anderson E., Francis C., 2012, *Astron. Lett.*, 38, 331  
 Anglada-Escudé G., Butler R. P., 2012, *ApJS*, 200, 15  
 Anglada-Escudé G. et al., 2013, *A&A*, 556, A126  
 Anglada-Escudé G. et al., 2014, *MNRAS*, 443, L89  
 Avila G., Kohler D., Araya E., Gilliotte A., Eckert W., 2004, in Moorwood A. F. M., Iye M., eds, *Proc. SPIE Conf. Ser. Vol. 5492, Ground-based Instrumentation for Astronomy*. SPIE, Bellingham, p. 669  
 Baluev R. V., 2009, *MNRAS*, 393, 969  
 Baluev R. V., 2012, *MNRAS*, 422, 2372  
 Barnes J. R., Collier Cameron A., Unruh Y. C., Donati J. F., Hussain G. A. J., 1998, *MNRAS*, 299, 904  
 Barnes J. R. et al., 2012, *MNRAS*, 424, 591  
 Berdiñas Z. M., Amado P. J., Anglada-Escudé G., 2015, in van Belle G. T., Harris H. C., eds, *18th Cambridge Workshop on Cool Stars, Stellar Sys-*

- tems, and the Sun also know as Cool Stars*. Flagstaff, Arizona, available at: <http://www2.lowell.edu/workshops/coolstars18/>  
 Böhm T. et al., 2015, *A&A*, 577, A64  
 Bouchy F., Isambert J., Lovis C., Boisse I., Figueira P., Hébrard G., Pepe F., 2009, in Kern P., ed., *EAS Publ. Ser. Vol. 37, Astrophysics Detector Workshop 2008*. EDP Sciences, Les Ulis, p. 247  
 Bourrier V., Hébrard G., 2014, *A&A*, 569, A65  
 Cosentino R. et al., 2012, in McLean I. S., Ramsay S. K., Takami H., eds, *Proc. SPIE Conf. Ser. Vol. 8446, Ground-based and Airborne Instrumentation for Astronomy IV*. SPIE, Bellingham, p. 84461V  
 Cumming A., 2004, *MNRAS*, 354, 1165  
 Donati J.-F., Semel M., Carter B. D., Rees D. E., Collier Cameron A., 1997, *MNRAS*, 291, 658  
 García-Gil A., Muñoz-Tuñón C., Varela A. M., 2010, *PASP*, 122, 1109  
 Hayes D. S., Latham D. W., 1975, *ApJ*, 197, 593  
 Jenkins J. S., Ramsey L. W., Jones H. R. A., Pavlenko Y., Gallardo J., Barnes J. R., Pinfield D. J., 2009, *ApJ*, 704, 975  
 Martins J. H. C., Figueira P., Santos N. C., Lovis C., 2013, *MNRAS*, 436, 1215  
 Mayor M. et al., 2003, *The Messenger*, 114, 20  
 Pepe F., Mayor M., Galland F., Naef D., Queloz D., Santos N. C., Udry S., Burnet M., 2002, *A&A*, 388, 632  
 Pepe F. et al., 2004, *A&A*, 423, 385  
 Pepe F. A. et al., 2010, in McLean I. S., Ramsay S. K., Takami H., eds, *Proc. SPIE Conf. Ser. Vol. 7735, Ground-based and Airborne Instrumentation for Astronomy III*. SPIE, Bellingham, p. 77350F  
 Pepe F. et al., 2011, *A&A*, 534, A58  
 Press W. H., 1992, *Numerical Recipes in Fortran 77: The Art of Scientific Computing: Fortran Numerical Recipes*. Cambridge Univ. Press, Cambridge (reprinted with corrections: 1996, 1997, 2001, 2003)  
 Probst R. A. et al., 2014, in Ramsay S. K., McLean I. S., Takami H., eds, *Proc. SPIE Conf. Ser. Vol. 9147, Ground-based and Airborne Instrumentation for Astronomy V*. SPIE, Bellingham, p. 91471C  
 Quirrenbach A. et al., 2014, in Ramsay S. K., McLean I. S., Takami H., eds, *Proc. SPIE Conf. Ser. Vol. 9147, Ground-based and Airborne Instrumentation for Astronomy V*. SPIE, Bellingham, p. 91471F  
 Reid I. N., Hawley S. L., Gizis J. E., 1995, *AJ*, 110, 1838  
 Reiniers A., Shulyak D., Anglada-Escudé G., Jeffers S. V., Morin J., Zechmeister M., Kochukhov O., Piskunov N., 2013, *A&A*, 552, A103  
 Scargle J. D., 1982, *ApJ*, 263, 835  
 Snellen I. A. G., de Kok R. J., de Mooij E. J. W., Albrecht S., 2010, *Nature*, 465, 1049  
 van Leeuwen F., 2007, *A&A*, 474, 653  
 Zechmeister M., Kürster M., 2009, *A&A*, 496, 577

## SUPPORTING INFORMATION

Additional Supporting Information may be found in the online version of this article:

**Table 2.** Radial velocities observed for GJ 725A and GJ 725B with HARPS-N.

(<http://www.mnras.oxfordjournals.org/lookup/suppl/doi:10.1093/mnras/stw906/-/DC1>).

Please note: Oxford University Press is not responsible for the content or functionality of any supporting materials supplied by the authors. Any queries (other than missing material) should be directed to the corresponding author for the article.

This paper has been typeset from a  $\text{\TeX}/\text{\LaTeX}$  file prepared by the author.